

## Effects of Al powder on the reaction process and reactivity of B/KNO<sub>3</sub> energetic sticks

Chen-yang Li<sup>a,b</sup>, Min-jie Li<sup>a,b</sup>, Hao-yu Song<sup>a,b</sup>, Chuan-hao Xu<sup>a,b</sup>, Lei Gao<sup>a,b</sup>, Bao-yun Ye<sup>a,b</sup>, Jing-yu Wang<sup>a,b</sup>, Chong-wei An<sup>a,b,\*</sup>

<sup>a</sup> School of Environment and Safety Engineering, North University of China, Taiyuan, 030051, China

<sup>b</sup> Shanxi Engineering Technology Research Centre for Ultrafine Powder, North University of China, Taiyuan, 030051, China

### ARTICLE INFO

#### Keywords:

B/KNO<sub>3</sub>

Direct ink writing (DIW)

Energetic stick

Reaction process

Flame propagation behavior

### ABSTRACT

Boron/potassium nitrate (B/KNO<sub>3</sub>) is a type of critical energetic composite material (ECM). However, the inert oxide layer on the B surface of B/KNO<sub>3</sub> hinders the contact between pure fuel and oxidant, thus limiting energy release. This limitation could be eliminated by adding highly reactive Al powder. To discern the effects of Al powder size on the reaction process and reactivity of B/KNO<sub>3</sub>, this study prepared Al/B/KNO<sub>3</sub>/polyvinylidene fluoride (PVDF) energetic sticks using the direct ink writing (DIW) technology. This study characterized the macroscopic morphology and structure of the energetic sticks using a laser scanning microscope and a scanning electron microscope, examined the reaction process of the composites using a differential scanning calorimeter and a thermogravimetric analyzer, and observed the flame propagation behavior of energetic sticks and energetic architectures using a high-speed camera. Furthermore, it tested the pressure output characteristics of the energetic composites using a closed volume tank. The results show that adding Al powder can improve the combustion efficiency of B/Al composite fuels and reduce the agglomeration of the combustion products. The Al powder with various particle sizes affects various reaction stages of the composite. The combustion and pressure output tests suggest that adding Al powder with a particle size of 1 μm yielded high reactivity and that flame jump propagation appeared in energetic architectures when the channel spacing was below 10 mm. These findings provide a guide for modifying the B/KNO<sub>3</sub> energetic composites and regulating the reactivity of energetic sticks.

### 1. Introduction

ECMs, which are generally composed of energetic materials, binders, and other additives, play a vital role in the energetic material field. They are extensively applied in fields such as modified explosives,<sup>1–5</sup> solid propellants,<sup>6–8</sup> nanothermites,<sup>9–11</sup> and semiconductor bridges (SCBs).<sup>12,13</sup> They hold critical significance in the multifunctional and multifield applications of energetic materials. Compared to ECMs for explosives (intramolecular energetic compounds composed of C, H, O, and N), intermolecular reactive composite materials, with fuel/oxidant mixed components as the research subject, enjoy significant advantages in energy density<sup>14,15</sup> and reactivity regulation scale.<sup>16</sup> Among all active fuels, boron (B) has a higher bulk energy density (136 kJ cm<sup>-3</sup>) and mass-energy density (58 kJ g<sup>-1</sup>) than other active metals,<sup>17,18</sup> frequently forming combustion systems with other components. These systems are widely used in solid propellants,<sup>19,20</sup> thermobaric explosives,<sup>21,22</sup> deep

spacecraft,<sup>23</sup> and gas generators.<sup>24</sup> The B/KNO<sub>3</sub> combination with a high calorific value and high stability is a representative.<sup>16,23</sup> However, the high melting point (2074 °C) and high boiling point (2550 °C) of B<sup>25,26</sup> necessitate high melting and vaporization temperatures. In other words, B can ignite only at a high temperature. Moreover, the low melting point (450 °C) and high boiling point (1860 °C) of boron oxide (B<sub>2</sub>O<sub>3</sub>) in the outer layer of B encapsulate B particles into liquid films during the combustion. This hinders the combustion of pure B particles, resulting in a long ignition time and incomplete combustion and thus impeding energy utilization.<sup>25–29</sup> Therefore, enhancing the ignition and combustion performance and energy-release capacity of energetic composites with B as fuel has become the focus of research.

Although the initial reaction temperature of a combustion system can be effectively reduced by adding fluororubber<sup>30,31</sup> and metal fluoride,<sup>32,33</sup> the addition of these inert substances decreases the combustion performance of the composite.<sup>32,34</sup> Some methods, such as the

\* Corresponding author. School of Environment and Safety Engineering, North University of China, Taiyuan, 030051, China.

E-mail address: [anchongwei@yeah.net](mailto:anchongwei@yeah.net) (C.-w. An).

<https://doi.org/10.1016/j.enmf.2023.10.004>

Received 8 June 2023; Received in revised form 8 August 2023; Accepted 14 October 2023

Available online 17 October 2023

2666-6472/© 2023 The Authors. Publishing services by Elsevier B.V. on behalf of KeAi Communications Co. Ltd. This is an open access article under the CC BY-NC-ND license (<http://creativecommons.org/licenses/by-nc-nd/4.0/>).

washed and surface-modified method,<sup>27</sup> the high-energy ball milling method,<sup>35</sup> and the electrostatic spraying method<sup>30,36</sup> have been employed to replace the conventional mechanical mixing process, thus improving the B reactivity. However, these methods suffer complex processes and low production efficiency. Adding high-reactivity metals to B-containing systems<sup>30,37–41</sup> has proven to be an effective way to overcome the poor ignition performance of boron fuel. Most especially, Al powder, characterized by a low price, high thermal conductivity, and strong reactivity, is frequently added to B-containing systems.<sup>30,41</sup> Nonetheless, micro- and nano-scale Al powders manifest distinct properties, specifically in terms of specific surface area, active Al content, melting point, and reaction activation energy, resulting in different reactivity and energy characteristics.<sup>42,43</sup> Although the above studies have confirmed that adding Al powder can enhance the ignition and combustion performance of B-containing systems, there is a lack of research on the effect of Al powder size on the reactivity of the systems. Similarly, the mechanism by which the Al powder size affects the reaction process of the composite system is still undefined.

Besides, the powder integration of ECMs is still challenging, although fuel/oxidant composites with high reactivity and energy density have been successfully prepared using methods such as advanced mechanical mixing,<sup>35,44</sup> the solvent/nonsolvent method,<sup>45,46</sup> the electrostatic spray method,<sup>47</sup> and the self-assembly method.<sup>48–50</sup> With the miniaturization and customization of energy devices, ECM powders fail to meet the fine-scale and arbitrary requirements of the charging process. Fortunately, additive manufacturing technologies allow for the customization and micro-size assembly of ECMs, such as propellants,<sup>51–53</sup> explosives,<sup>54–57</sup> and nanothermites.<sup>34,58–64</sup> Among these technologies, the direct ink writing (DIW) technology, enjoying high dimensional freedom, high processing efficiency, and low cost, serves as a major charging method for micro detonation devices<sup>55,56</sup> and microenergy release structures.<sup>16,61,62</sup> With energetic particles as the principal part and binder as the skeleton, the DIW can achieve the orderly deposition of ECMs according to the preset program<sup>16</sup> and the multidimensional formation of one-dimensional sticks, two-dimensional networks, and three-dimensional structures. Among them, energetic sticks are the basic unit. Therefore, it is particularly critical to study the energy release characteristics of ECMs in a linear state. However, there is a lack of such studies since most of research on B/Al-containing systems focuses on composite material powders.<sup>30,41</sup>

In this study, Al/B/KNO<sub>3</sub>/PVDF energetic ink was prepared using a planetary mixer, with amorphous B as fuel, potassium nitrate (KNO<sub>3</sub>) as an oxidant, PVDF as a binder, and Al powders with different particle sizes (1  $\mu\text{m}$ , 50 nm) as additives. Based on this, Al/B/KNO<sub>3</sub>/PVDF energetic composite sticks with different Al particle sizes and Al contents were prepared using a visual DIW device. Their macroscopic and microscopic morphologies were characterized. Furthermore, their linear combustion properties and pressure output were studied, obtaining the Al content vs. linear burning rate curves. The decomposition processes of different Al/B/KNO<sub>3</sub>/PVDF ECMs were studied using the thermal analysis technology, followed by the revealing of the effects of different particle sizes and contents of Al powder on the peak temperature, enthalpy, and temperature range during the system reaction. Additionally, the flame propagation behavior of energetic architectures was explored. These efforts reveal the mechanism by which Al powder size influences the reactivity of Al/B/KNO<sub>3</sub>/PVDF energetic sticks and the reaction process of ECMs, assisting in research the energy-release capacity of energetic composite sticks.

## 2. Experimental section

### 2.1. Chemicals

Amorphous B, with an average particle size of about 1  $\mu\text{m}$ , was purchased from Nangong Bole Metal Materials Co., Ltd., China. Al powders, with different particle sizes (about 50 nm and 1  $\mu\text{m}$ ), were

purchased from Flance (Beijing) Nanotechnology. The particle size distribution and SEM images of all the metal particles are shown in Fig. S1. KNO<sub>3</sub> was purchased from Chengdu Kelong Chemicals Co., Ltd., China. Ultrafine KNO<sub>3</sub>, with an average particle size of about 5  $\mu\text{m}$ , was prepared using the nozzle-assisted simultaneous precipitation (NASP) method. The solvent was purified water, and the non-solvent was anhydrous ethanol (Energy Chemical, China). PVDF (MW = 1,100,000) was purchased from Arkema, France, and N, N-dimethylformamide (DMF, 99.8 %) was purchased from Tianjin Shentai Chemical Reagent Co., Ltd.

### 2.2. Preparation and combustion of B/Al composites

A certain amount of B and Al powders (Table S1) were mixed with an appropriate amount of ethanol using a planetary mixer. Then, B/Al composites were obtained through filtration and drying. The combustion experiments of the powders were carried out in a quartz tube filled with oxygen, as shown in Fig. S1 a. The oxygen flow was maintained for 2 min at a rate of 5 L min<sup>-1</sup> to ensure that the quartz tube was filled up with oxygen. The mass of the composites was 50 mg in each experiment. The composites were ignited using a Joule-heated Ni–Cr wire, and the power supply voltage was set to 3 V.

### 2.3. Preparation and DIW processes of energetic ink

The preparation and DIW processes of energetic inks are shown in Fig. 1. A certain amount of PVDF was dissolved in DMF, followed by magnetic stirring for 5 h to ensure complete dissolution. To ensure a uniform distribution, a planetary mixer was utilized to mix in a stepwise manner. The principle is that the turntable rotated around the center line of the equipment, while the container with inks on the turntable autorotated concurrently, producing a strong vortex ink flow. The shear force between the inks and the wall, as well as the interactions between the particles, made each component of the inks evenly dispersed. KNO<sub>3</sub> was added to the PVDF solution and mixed for 90 s at a rate of 1500 rpm in the planetary mixer. Then, Al and B were added in turn and mixed in the same way. Al/B/KNO<sub>3</sub>/PVDF inks with different Al particle sizes were prepared, and all formulations followed Table S2. The rheological properties of the inks were tested using an MCR 302 rheometer. The shear rate ranged from 0.1 to 50 s<sup>-1</sup>, with 50 test points set.

The inks were loaded into a syringe, which was then fixed to the DIW device. The pressure was set at 0.03–0.05 MPa to ensure that the inks could pass evenly through the needle (outer diameter: 0.98 mm). The temperature of the substrate was set to 75 °C to ensure solvent evaporation from the inks. In this study, energetic sticks were prepared through layer-by-layer stacking of energetic films, each of which had an average thickness of about 100  $\mu\text{m}$ . Each energetic stick was superimposed by 10 layers of energetic films, thus obtaining a cross-section of approximately 1 mm  $\times$  1 mm.

### 2.4. LSM, SEM-EDS, XRD, DSC–TG, and pressure output tests

The macroscopic morphology of energetic sticks was characterized using an LSM-900 laser scanning microscope (Carl Zeiss, Germany) to obtain the sections and 3D images of the sticks. The microstructure of the energetic sticks was observed using an S4700 scanning electron microscope (Hitachi, Japan), and the distribution uniformity of energetic sticks was characterized using an energy dispersive spectrometer (Oxford Xplore, Britain). The composition of energetic composites was determined using a DX-2700 X-ray diffractometer (Dandong Haoyuan Instrument Co., Ltd., China). The thermal decomposition properties and reaction processes of the energetic composites were analyzed using a differential scanning calorimeter (Setaram, France) and a TGA 2 thermogravimetric analyzer (Mettler Toledo, Switzerland). The pressure-time curves were obtained through a combustion experiment using a 20 mL closed volume tank. A total of 5-mg-weight samples were

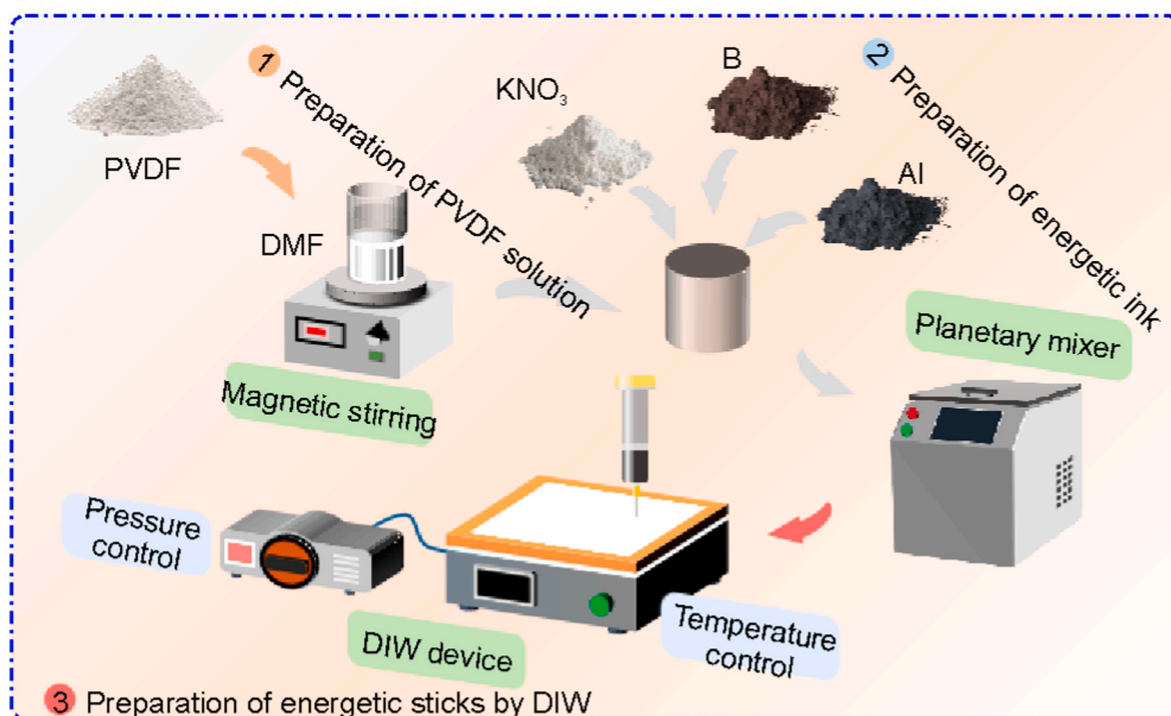


Fig. 1. Preparation and DIW processes of Al/B/KNO<sub>3</sub>/PVDF energetic inks.

weighed and ignited using a Ni–Cr wire with a diameter of 0.25 mm.

## 2.5. Combustion process of energetic sticks

The flame propagation of energetic sticks during burning was tracked using an i-SPEED 221 high-speed camera (iX Cameras, UK). In a typical experiment, a 1 mm × 1 mm × 30 mm energetic stick was fixed within an explosion-proof box equipped with a filming window and was then ignited using a Joule-heated Ni–Cr wire (Fig. S2 b), which was powered by a VICTOR 3003 A DC Regulated power supply (Shenzhen Yisheng Shengli Technology Co., Ltd., China) to generate heat. To

ensure consistent ignition energy, the power supply's voltage was set to 3 V. After the energetic stick was ignited, the flame propagated forward. The ignition point of the energetic stick was set as the origin of the coordinate. The distance from the flame front to the origin was considered as the flame displacement ( $X_n$ ; Fig. S2e). With the Image J software, the displacement-time curve of the flame was derived, and the linear burning rate of the energetic stick was calculated.

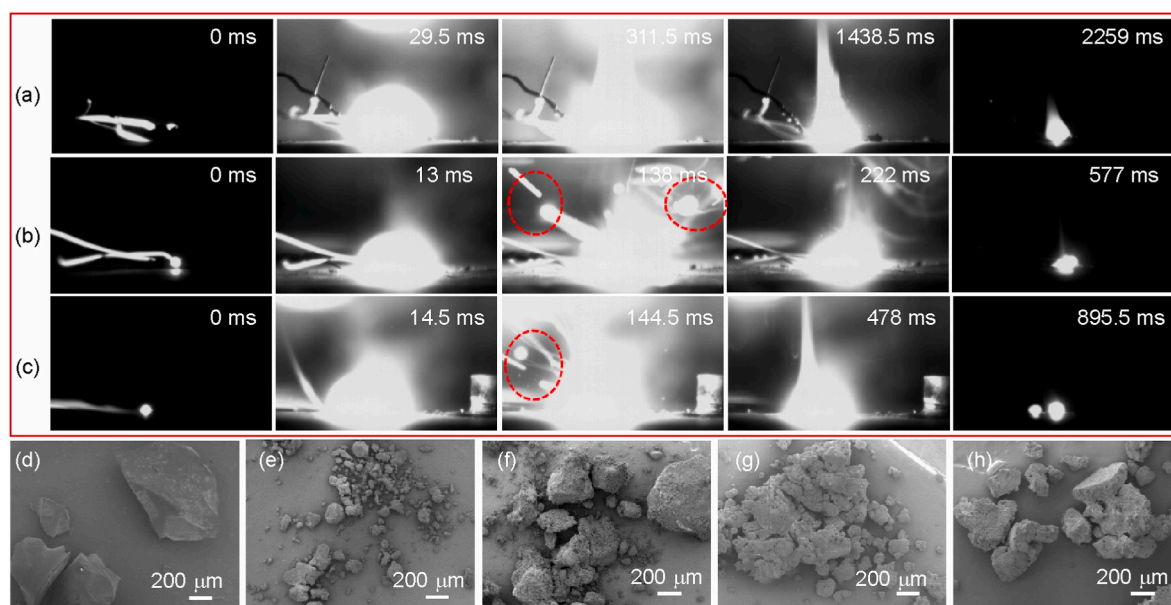


Fig. 2. Combustion and oxidation processes of fuels. Burning snapshots of B powder (a), nano-Al/B composites (b), and micro-Al/B composites (c); SEM images showing the combustion products of B powder (d), nano-Al (e), micro-Al (f), nano-Al/B composites (g), and micro-Al/B composites (h).



### 3. Results and discussion

#### 3.1. Combustion and oxidation characteristics of B/Al composites

Fig. 2a–c depict the combustion processes of B powder, B/Al composites with 10 wt% nano-Al powder, and B/Al composites with 10 wt% micro-Al powder, respectively. The B powder had a long combustion time (2259 ms) and reached the maximum flame area (311.5 ms) after a long time. The addition of Al powder significantly shortened the combustion time of the composite. Unlike the combustion of B particles (Fig. 2a), when the composites containing nano-Al particles (Fig. 2b) reached the maximum flame area, the particles were observed spraying outward. This was caused by the melt dispersion mechanism of the nano-Al powder. The melting of the Al core increased the internal pressure of the particles and then caused the alumina shell to break.<sup>65,66</sup> The spattered Al droplets burned, and thus the high-boiling-point oxide shell of the B outer layer was removed in advance, increasing the burning rate of the composite. The same phenomenon was also observed during the combustion of the composites containing micro-Al (Fig. 2c), and the broken alumina shell was found in the SEM images of the combustion products of the micro-Al powder (Fig. S3a), suggesting that 1  $\mu\text{m}$  micro-Al powder exhibited the reaction characteristics of the nano-Al powder. The addition of 1  $\mu\text{m}$  micro-Al powder increased the burning rate of the composite, although the combustion duration (895.5 ms) and the time when the flame area peaked (144.5 ms) were longer than those of the composites containing nano-Al.

Fig. 2d–h demonstrate the SEM images of the products. The combustion products (Fig. 2d) of B were large irregular agglomerates. During the combustion, the  $\text{B}_2\text{O}_3$  oxide layer around B melted and wrapped the pure B due to its low melting point and high boiling point, thus hindering the reaction between B and oxygen and reducing the combustion efficiency. Consequently, the molten oxide condensed rapidly post-combustion, forming large agglomerates. In contrast, the combustion products of Al (Fig. 2e and f) were less agglomerated. The combustion products of B/Al composites exhibited weakened agglomeration (Fig. 2g and h) due to the 10 wt% Al added. The combustion of Al eliminated the limitation of the  $\text{B}_2\text{O}_3$  oxide layer. Consequently,  $\text{B}_2\text{O}_3$  reacted with  $\text{Al}_2\text{O}_3$  at a high temperature, forming aluminum borate

whiskers<sup>67</sup> (including  $\text{AlBO}_3$ , and  $\text{Al}_4\text{B}_2\text{O}_9$ ), as shown in Fig. S3 b–c. The initial reaction temperatures of the fuels were obtained through TG-DTG tests, as shown in Fig. 3, which reveals a two-stage oxidation process of single metals and a three-stage oxidation process of the composites with 10 wt% Al powder. The initial reaction temperatures of B, nano-Al, and micro-Al were 608.18  $^\circ\text{C}$ , 533.62  $^\circ\text{C}$ , and 563.71  $^\circ\text{C}$ , respectively. The initial reaction temperatures of the composites with nano-Al (568.5  $^\circ\text{C}$ ) and micro-Al (589.02  $^\circ\text{C}$ ) powder were significantly lower than that of B powder because Al had higher reactivity than B and reacted with oxidant before B.

#### 3.2. Rheological properties and DIW of B/Al/ $\text{KNO}_3$ /PVDF energetic inks

Al/B/ $\text{KNO}_3$ /PVDF energetic inks were prepared through stepwise mixing. Fig. 4a showcases the mixing results of inks after  $\text{KNO}_3$ , B, and Al were added. All the inks displayed smooth surfaces, without agglomeration. The rheological properties of the inks were tested, as shown in Fig. 4b and c. All the energetic inks possessed strong shear-thinning characteristics, which was essential for their extruded and patterned deposition. At a lower shear rate ( $<30 \text{ s}^{-1}$ ), the viscosity of the inks tended to increase as the particle size of the Al power decreased. A smaller particle size corresponded to a larger specific surface area, thus increasing the contact area between solid particles. The friction between particles subjected to shear increased, increasing the viscosity of the inks. Similarly, the viscosity of the inks also increased as the amount of Al increased.

The DIW technology allowed for the deposition on demand of the energetic inks as energetic sticks (Fig. 4 d), achieving the powder integration of energetic composites. The sticks showed an approximately rectangular cross-section (Fig. 4e) with both a width and a thickness of about 1 mm. The 3D image of the energetic stick (Fig. 4f) shows a smooth surface and a regular shape, indicating that the DIW technology allows for the formation of energetic sticks with excellent forming effects. In addition, all energetic sticks displayed a consistent size, which is crucial to research on the reactivity of different energetic sticks. The honeycomb pattern was prepared using the DIW technique and Al/B/ $\text{KNO}_3$ /PVDF inks containing nano-Al addition, as shown in Fig. 4g. This pattern suggests that viscoelastic inks with shear-thinning properties

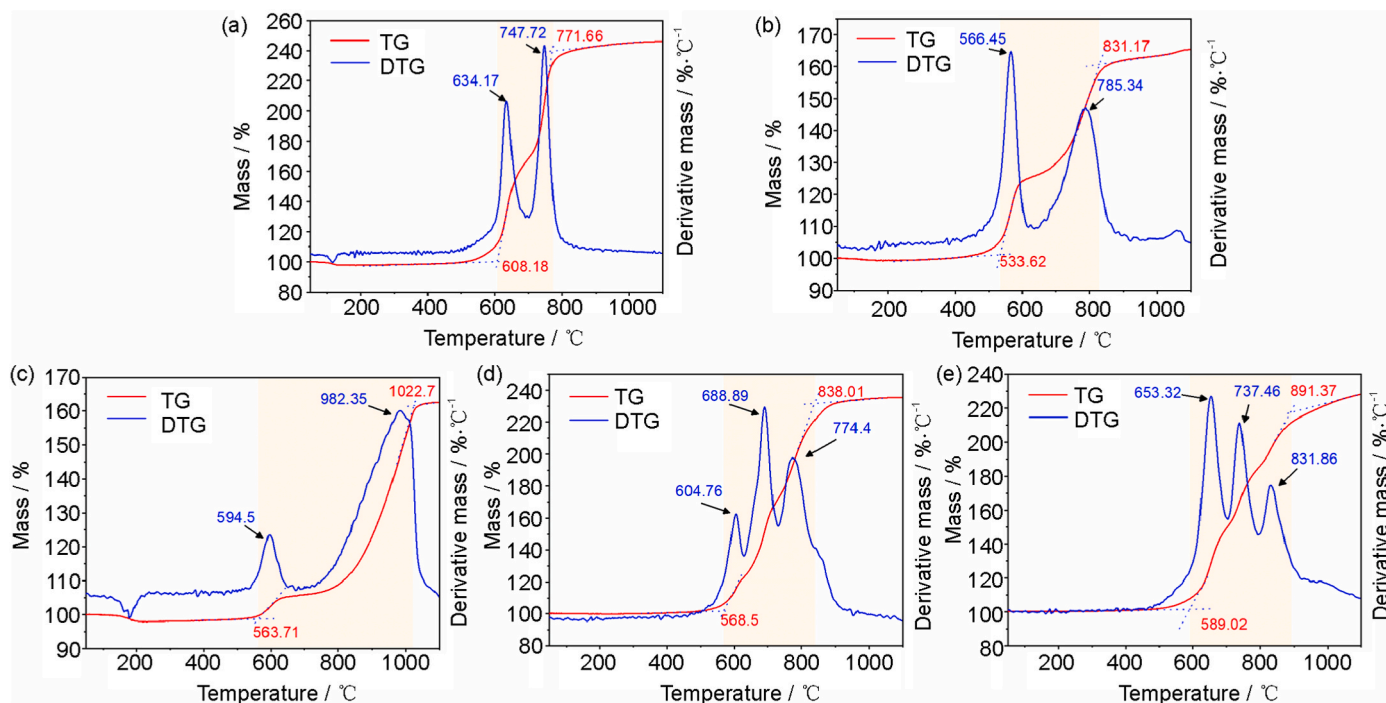
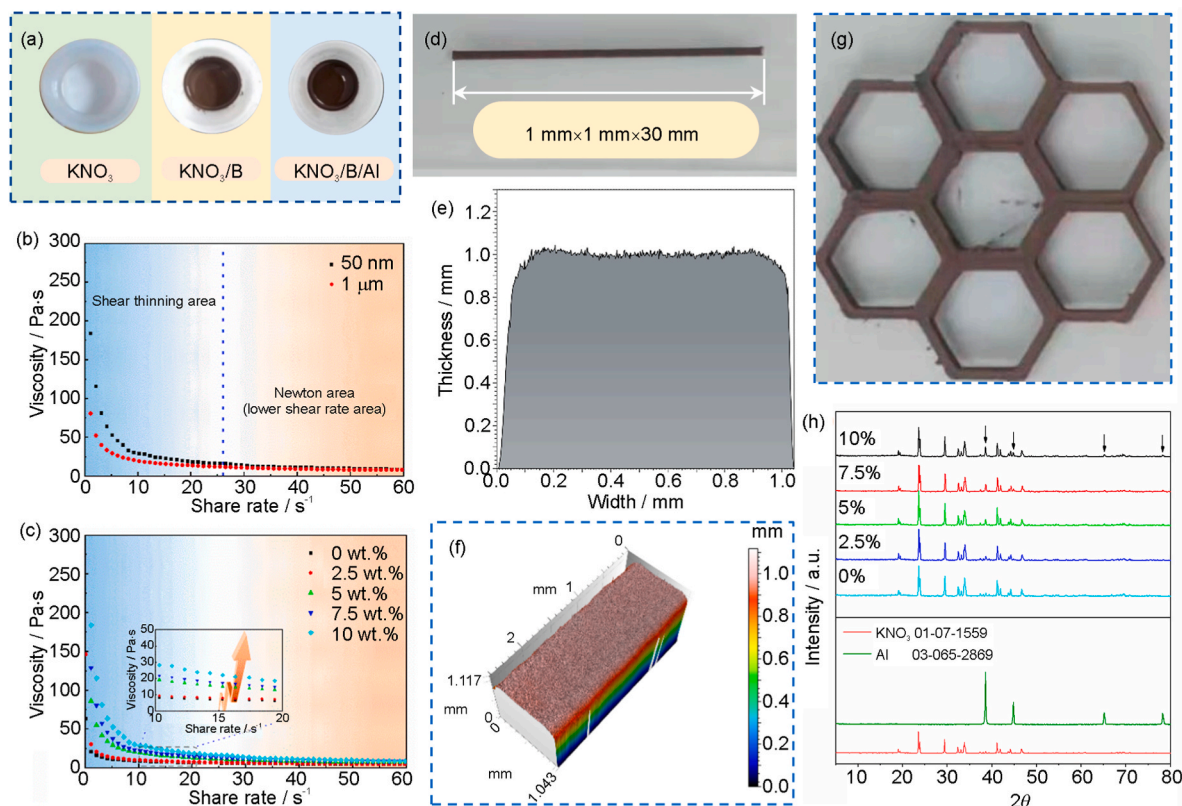


Fig. 3. TG-DTG curves of B powder (a), nano-Al (b), micro-Al (c), nano-Al/B composites (d), and micro-Al/B composites (e).





**Fig. 4.** Direct ink writing of energetic inks. Optical images of energetic inks obtained through stepwise mixing (a); Shear rate-viscosity curves of energetic inks with 10 wt % different Al particle sizes (b); Shear rate-viscosity curves of energetic inks with different 50 nm Al contents (c); Optical image (d), cross-section profile (e), and 3D image (f) of an energetic stick with 10 wt % 50 nm Al powder; Optical image of a honeycomb network structure prepared using the DIW technology and containing 10 wt % 50 nm Al powder (g); XRD results of samples with different Al contents and an Al particle size of 50 nm (h).

made it possible to prepare complex network structures, which is critical for achieving the orderly deposition of energetic arrays in micro-energy devices. The characteristic peaks for composites emerged as a combination of the characteristic peaks of Al and  $\text{KNO}_3$ , with the intensity of the characteristic peaks of Al decreased as the Al content decreased (Fig. 4h). Due to the use of amorphous B, the XRD pattern did not showcase the characteristic peak of B.

### 3.3. Morphologies of B/Al/ $\text{KNO}_3$ /PVDF energetic sticks

The distribution of reactant components and the energy release of energetic composites are strongly connected.<sup>61</sup> Especially for energetic sticks with small diameters, the uniformity of their composition has a significant influence on their combustion performance. When the reactants are uniformly distributed, the fuel is in full contact with oxidant particles, resulting in more complete and rapid reactions of B/Al with  $\text{KNO}_3$  and a higher energy output. Therefore, it is crucial to ensure a homogeneous mixing of energetic components.

Fig. 5a and b shows the SEM images of energetic sticks containing 10 wt % micro-Al powder, indicating that the Al powder did not agglomerate. Fig. 5c–f depict the SEM images of energetic sticks containing nano-Al powder. Notably, the nano-Al powder (Fig. 5e and f) proved more susceptible to agglomeration than the micro-Al powder. Fig. 5g and h show the EDS diagrams of the cross-sections of energetic sticks containing 50 nm and 1  $\mu\text{m}$  Al powder (10 wt%), respectively. The Al element (orange) represents the distribution of nano-Al powder, and the B (cyan), K (purple), and F elements (green) represent the distribution of amorphous B, ultrafine  $\text{KNO}_3$ , and PVDF, respectively. The EDS results show that the nano-Al powder showed agglomeration behavior (Fig. 5g) compared to the energetic sticks containing 1  $\mu\text{m}$  Al powder (Fig. 5h). Although the homogeneity of the composites was significantly improved

by mixing with a planetary mixer, the physical mixing method cannot fundamentally address the problem of the agglomeration of nano-powders. In addition, the SEM images (Fig. S4) and EDS images (Fig. S5) of energetic sticks with different Al contents (1  $\mu\text{m}$ ) also showed the uniform distribution of various components.

### 3.4. Thermal decomposition of Al/B/ $\text{KNO}_3$ /PVDF energetic sticks

The DSC curves of Al/B/ $\text{KNO}_3$ /PVDF energetic composites are shown in Fig. 6a and b. The first endothermic peak emerged at 142.71  $^{\circ}\text{C}$ , representing the crystal transformation of  $\text{KNO}_3$ . The second endothermic peak appeared at 337.92  $^{\circ}\text{C}$ , representing the melting of  $\text{KNO}_3$ . These curves were consistent with the DSC curve of the B/ $\text{KNO}_3$ /PVDF energetic composites (Fig. S6 a), which shows three decomposition exothermic peaks. The first peak represented the decomposition of PVDF and the reaction of its decomposition product with metals, metal oxide layers, or oxidants. The second and third peaks represented the two stages of the B/ $\text{KNO}_3$  reaction because the MS equipment captured NO ( $m/z = 30$ , Fig. S6 b) between 400  $^{\circ}\text{C}$  and 500  $^{\circ}\text{C}$ . In addition, TG-DTG images also clearly indicate the two stages of the main reaction (Fig. S7). As the Al-F or the Al-O reactions released heat, the first and second exothermic peaks were superimposed, forming an exothermic peak after the Al powder was added. The difference was that the peak temperature of the exothermic peak and the reaction enthalpy varied with the particle size and Al content. These results are shown in Fig. 6c and d, where  $T$  and  $E$  represent the peak temperature and reaction enthalpy, respectively, the numbers immediately following  $T$  and  $E$  represent the first or second exothermic peak, and the last numbers represent the particle size of Al.

In the first reaction stage of Al/B/ $\text{KNO}_3$ /PVDF, the peak reaction temperature slightly changed after micro-Al powder was added

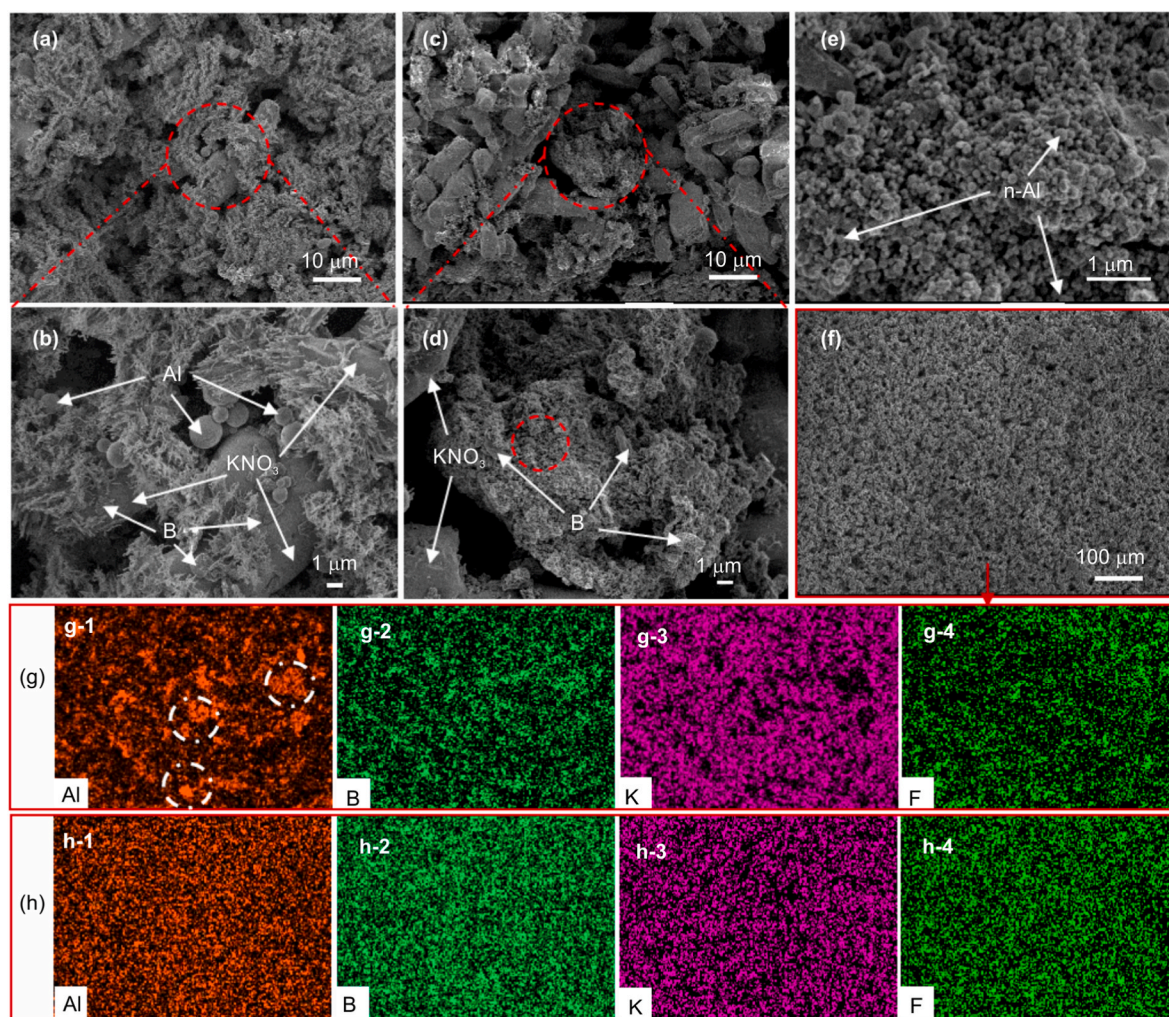


**Fig. 5.** SEM images of cross sections of Al/B/KNO<sub>3</sub>/PVDF energetic sticks with different Al particle sizes at different magnifications. The particle sizes of Al are 1 μm (a–b), and 50 nm (c–f); EDS images of energetic sticks containing 10 wt% 50 nm Al powder (g), and EDS images of energetic sticks containing 10 wt% 1 μm Al powder (h).

compared to that of the B/KNO<sub>3</sub>/PVDF composites (461.31 °C). In contrast, the addition of nano-Al with content over 2.5 wt% can reduce the peak reaction temperature. In instances where the nano-Al content was 10 wt%, the reaction temperature in the first stage was reduced to 443.6 °C. In the second reaction stage, the addition of 1 μm and 50 nm Al powder with a content of 10 wt% decreased the peak reaction temperature to 479.65 °C and 487.64 °C, respectively compared to that of the B/KNO<sub>3</sub>/PVDF composites (496.4 °C). This is closely related to the reaction characteristics of Al powder with different sizes. As shown in Fig. 3c, the oxidation reaction of micro-Al powder was concentrated between 800 °C and 1000 °C, with only a small number of particles oxidized between 600 °C and 800 °C. Therefore, the addition of micro-Al could not significantly reduce the peak temperature of the first reaction stage but had a significant effect on the peak temperature of the second reaction stage. In contrast, nano-Al was almost completely oxidized between 500 °C and 800 °C (Fig. 3b). Therefore, the addition of nano-Al powder had a great influence on the peak temperature of the first reaction stage. Similarly, the changes in reaction enthalpy showed the same trend (Fig. 6d). The addition of micro-Al significantly increased the enthalpy of the second reaction stage, while the addition of nano-Al greatly increased the enthalpy of the first reaction stage. In the first reaction stage, the reaction enthalpy increased from 290.31 J g<sup>-1</sup> to 1319.91 J g<sup>-1</sup> when 10 wt% nano-Al was added. In the second reaction stage, the reaction enthalpy of the composites reached 1821.16 J g<sup>-1</sup>

when 10 wt% micro-Al was added. In contrast, the addition of nano-Al did not significantly increase the reaction enthalpy of the second reaction stage. The reason is that nano-Al greatly promoted the exothermic reaction of the first stage, causing the reaction to be more prone to occur at a lower temperature.

The TG-DTG test results are shown in Fig. S8. Fig. 6e and f shows the variations in the initial temperature, the end temperature, and the reaction temperature range of the reaction of the energetic composites with different Al contents. The reaction temperature range could effectively account for the reaction efficiency of energetic composites. Specifically, a smaller reaction temperature range corresponded to higher reaction efficiency. The addition of low-content Al (2.5 wt%) neither shortened the temperature range of the reaction nor intensified the reaction process of the composite. Compared to the B/KNO<sub>3</sub>/PVDF energetic composites, the Al/B/KNO<sub>3</sub>/PVDF composites exhibited a significantly reduced reaction temperature range in instances where the micro-Al powder content was over 5 wt%, suggesting that its reaction efficiency was improved. In contrast, the addition of nano-Al powder did not significantly reduce the reaction temperature range of the Al/B/KNO<sub>3</sub>/PVDF composites but significantly decreased the temperature at the end of the reaction (Fig. 6f).

Although Al powder with different particle sizes affected different reaction stages of energetic composites, the addition of a certain amount of Al powder improved the reaction enthalpy and efficiency of energetic



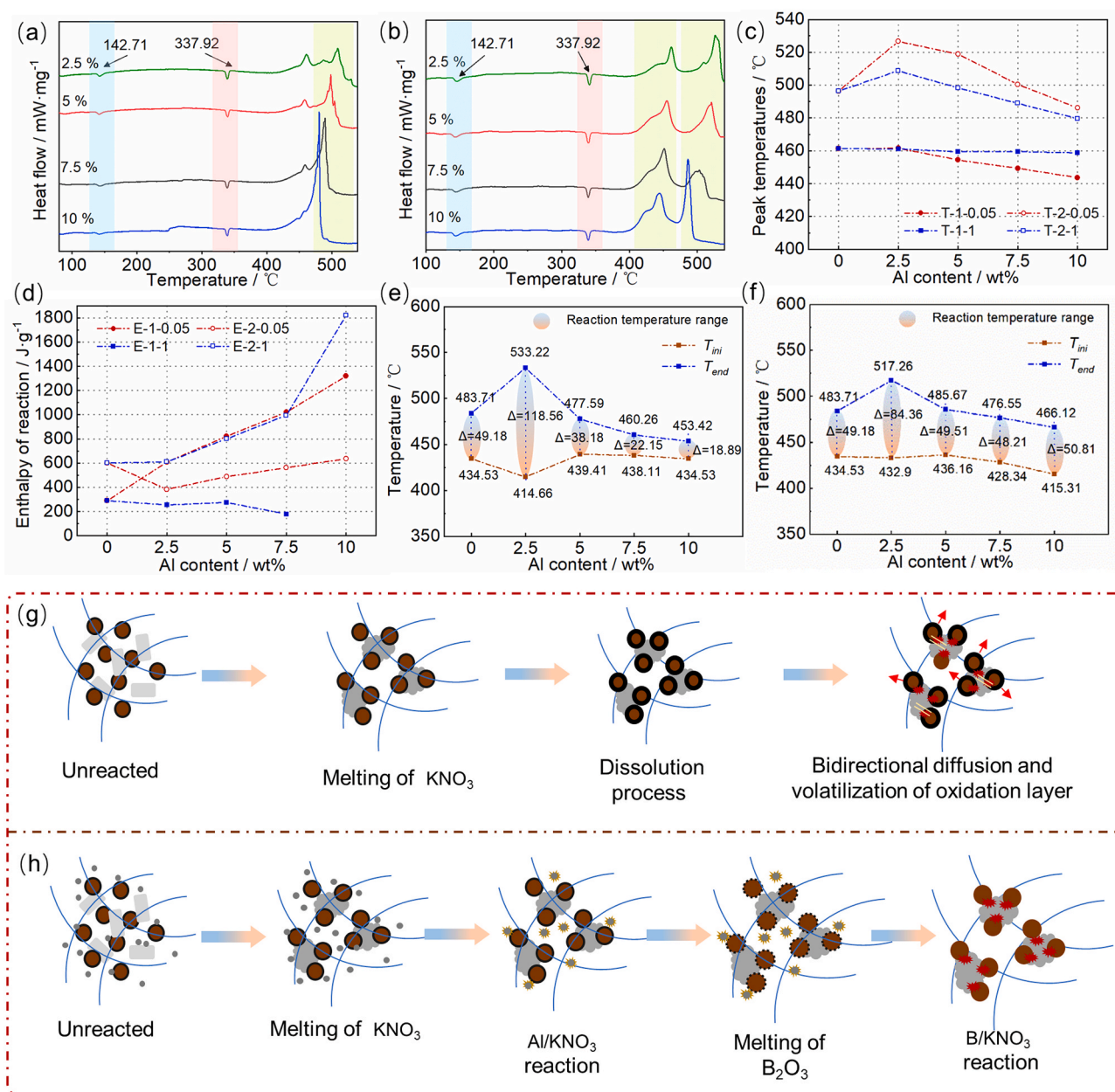


**Fig. 6.** DSC curves of Al/B/KNO<sub>3</sub>/PVDF energetic composites with Al particle sizes of 1 μm (a) and 50 nm (b); the peak temperature (c) and enthalpy of reaction (d) of different energetic composites; the reaction temperature ranges of energetic composites with Al particle sizes of 1 μm (e) and 50 nm (f); The reaction process diagrams of B/KNO<sub>3</sub>/PVDF (g) and Al/B/KNO<sub>3</sub>/PVDF (h) energetic composites.

composites. This implies enhanced reactions of the composites. The reaction process of B/KNO<sub>3</sub>/PVDF energetic composites was completed by the B-O diffusion of B particles and molten KNO<sub>3</sub> (Fig. 6g). In other words, at a certain temperature, B dissolved in molten B<sub>2</sub>O<sub>3</sub>, forming (BO)<sub>n</sub> liquid films, which diffused outward and reacted with O. Concurrently, O diffused inward and reacted with B. Experiments have shown the coexistence of this bilateral diffusion,<sup>68–70</sup> suggesting that the molten oxide layer continuously thickened during the reaction. This coexistence is unfavorable for the ignition and combustion of energetic composites. After adding a certain amount of Al powder, Al reacted with KNO<sub>3</sub> before B and released heat due to its higher reactivity.<sup>41</sup> As a result, the high boiling point of the inert B<sub>2</sub>O<sub>3</sub> oxide layer could be removed at a high temperature, and pure B particles could be exposed and participate in the oxidation reaction (Fig. 6h). Therefore, the

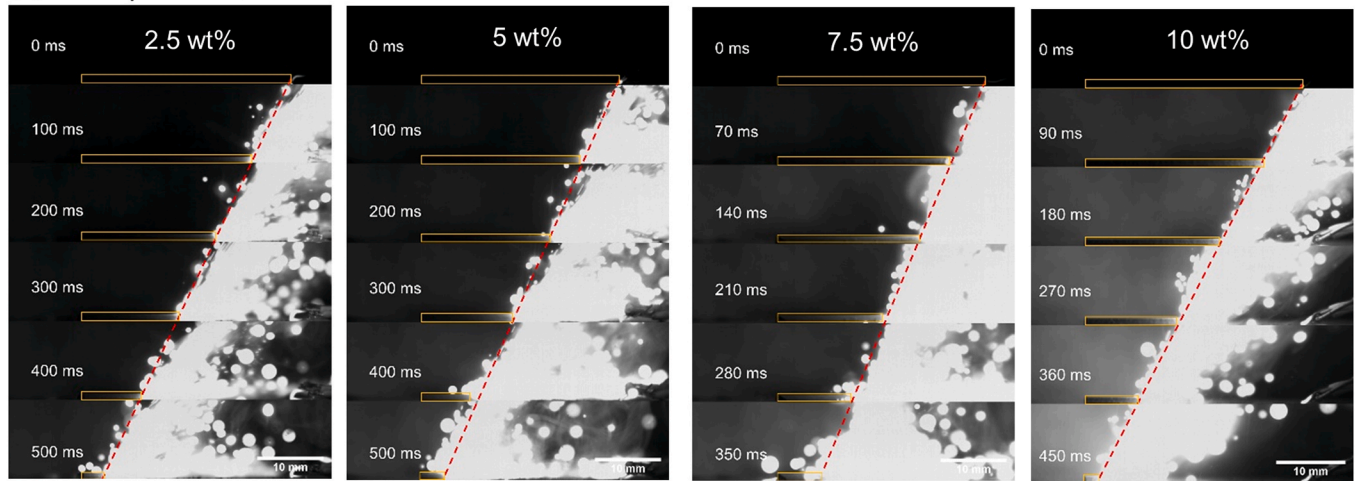
ignition characteristic of the composites was improved.

### 3.5. Combustion performance and pressure output of energetic sticks

Stable flame propagation is of great significance to the reliable energy output of energetic sticks. Fig. 7a and b shows the combustion process of Al/B/KNO<sub>3</sub>/PVDF energetic sticks with different Al particle sizes and different Al contents. All energetic sticks exhibited steady forward flame propagation and consistent linear burning rates during their combustion. The flames of the energetic sticks with micro-Al powder diffused forward and backward. In the combustion process of the energetic sticks with nano-Al powder, bright particles ejected outward more significantly although the flames weakened. This phenomenon is related to the combustion characteristics of the nano-Al powder



## (a) Composites with micro-Al added



## (b) Composites with nano-Al added

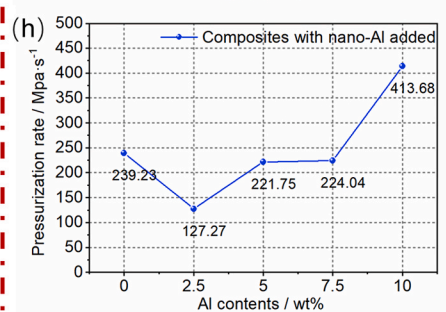
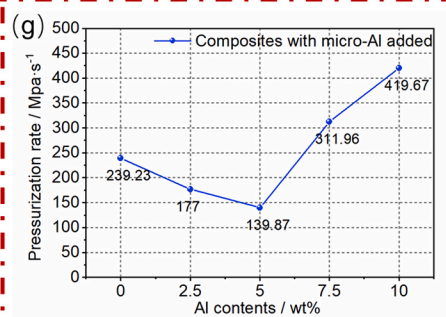
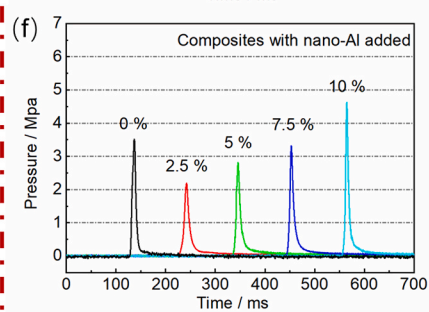
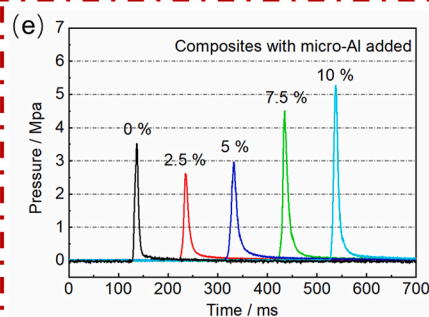
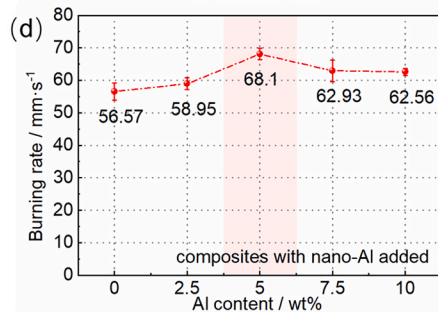
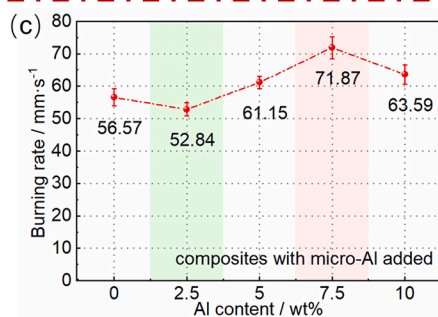
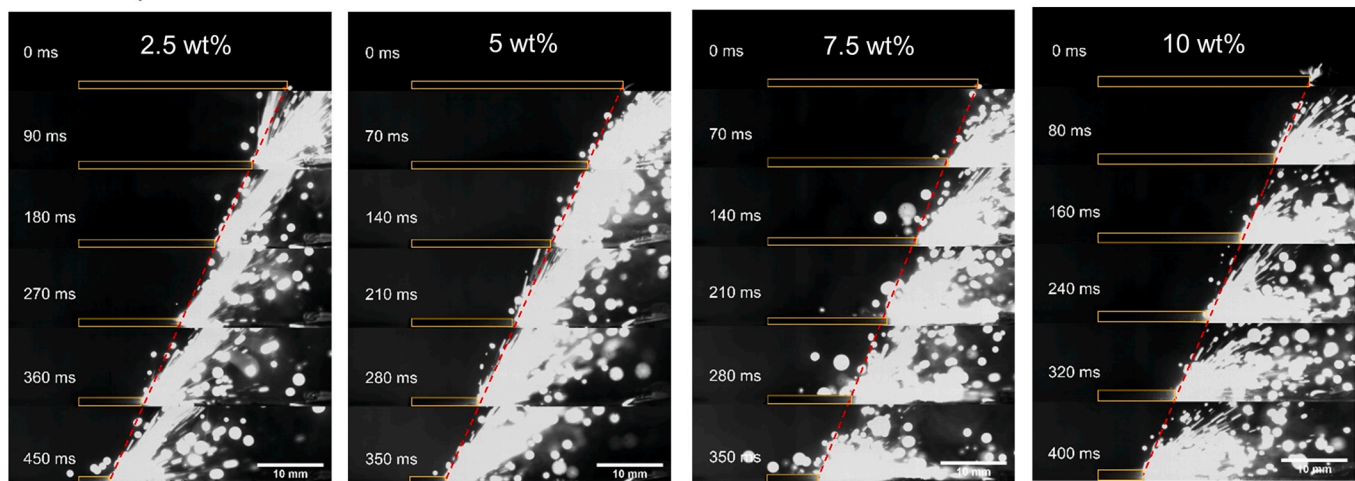


Fig. 7. Burning snapshots (a–b), burning rate vs. Al content curves (c–d), pressure vs. time curves (e–f), and pressurization rate vs. Al content curves (g–h) of Al/B/ $\text{KNO}_3$ /PVDF energetic sticks with different Al particle sizes.

and is consistent with the combustion of B/Al composites.

The burning rates of all the sticks are shown in Fig. 7c and d. When the Al particle size was 1  $\mu\text{m}$ , the linear burning rate showed a decreasing-increasing-decreasing trend with an increase in the Al content, reaching its minimum value when the Al content was 2.5 wt% ( $52.84 \text{ mm s}^{-1}$ ) and peaking when the Al content was 7.5 wt% ( $71.87 \text{ mm s}^{-1}$ ). When the Al particle size was 50 nm, the linear burning rate increased first and then decreased with an increase in Al content, peaking when the Al content was 5 wt% ( $68.1 \text{ mm s}^{-1}$ ). Owing to the large specific surface area of nano-Al powder and the strong reaction with oxidant, the burning rate vs. Al content curve of energetic sticks containing 50 nm Al powder lacked troughs. However, the energetic

sticks containing nano-Al did not show more advantages in linear burning rate than those with micro-Al. This may be caused by the agglomeration of nano-Al powder or may be related to the reaction path of Al powder with different particle sizes: 1  $\mu\text{m}$  Al powder also has the characteristics of the melt dispersion mechanism but has higher effective Al content than nano-Al powder.

The addition of Al powder significantly affected the pressure output. As shown by the pressure release test results of different composites (Fig. 7e–h), the pressure and pressurization rate decreased first and then increased with an increase in the Al content (for both 50 nm Al powder and 1  $\mu\text{m}$  Al powder). Both composites containing 1  $\mu\text{m}$  Al powder and those with 50 nm Al powder showed peak pressure release and

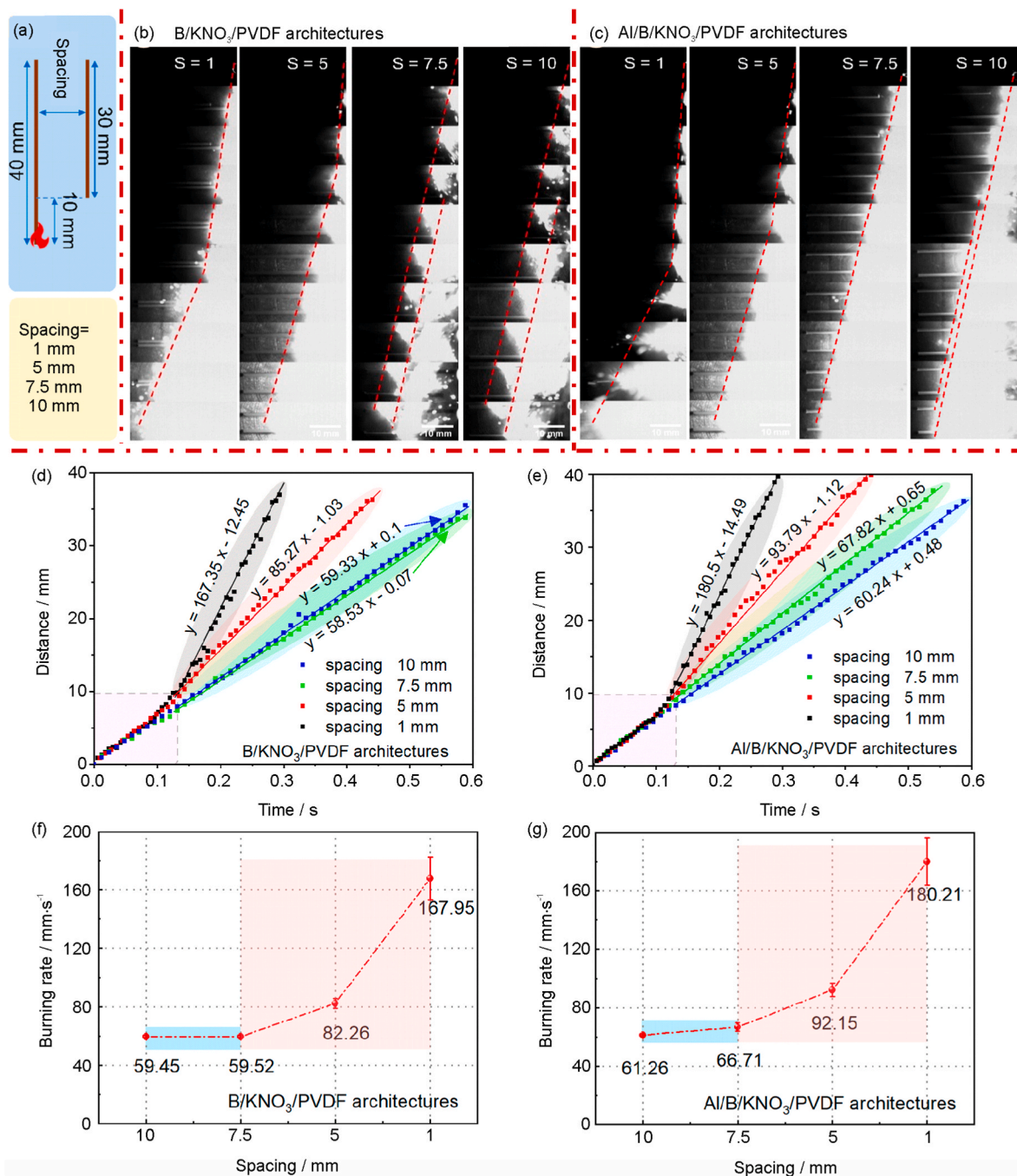


**Fig. 8.** Schematic diagram of the architecture with different spacing (a). Burning snapshots of B/KNO<sub>3</sub>/PVDF (b) and Al/B/KNO<sub>3</sub>/PVDF (c) architectures with different spacing. The flame distance vs. time curves of B/KNO<sub>3</sub>/PVDF (d) and Al/B/KNO<sub>3</sub>/PVDF (e) architectures with different spacing. Linear burning rates of B/KNO<sub>3</sub>/PVDF (f) and Al/B/KNO<sub>3</sub>/PVDF (g) architectures with different spacing.



pressurization rate when the Al content was 10 wt %, with the former exhibiting higher values (5.27 MPa, 419.67 MPa s<sup>-1</sup>) than the latter (4.63 MPa, 413.68 MPa s<sup>-1</sup>). This was also related to the reaction path of Al powders with different particle sizes.

### 3.6. Flame propagation behavior of architectures

Generally, flames linearly propagated along the energetic sticks. However, they would jump to the adjacent energetic sticks when the energetic sticks were arranged close, resulting in unconventional rapid combustion (Fig. S9). This jump propagation behavior is extremely dangerous for the storage and use of energetic materials. However, this rapid combustion phenomenon can also be used to regulate the reactivity of energetic arrays,<sup>16,71,72</sup> which is critical to the study of the energy-release effect of micro-energetic devices. The architectures of energetic sticks with different spacings were prepared using B/KNO<sub>3</sub>/PVDF energetic inks and Al/B/KNO<sub>3</sub>/PVDF energetic inks containing 1 μm Al powder (10 wt%), as shown in Fig. 8a. A Joule-heated Ni–Cr wire was employed to ignite long energetic sticks (40 mm), and a high-speed camera was utilized to record the flame jump phenomenon and the flame propagation behavior between adjacent energetic sticks.

Fig. 8b shows the flame propagation process of B/KNO<sub>3</sub>/PVDF energetic architectures. When the spacing between energetic sticks was below 10 mm, all flames jumped and ignited the adjacent sticks. They showed two successively propagating flame fronts when the spacing was wider than 7.5 mm, while two flame fronts merged into a larger flame front when the spacing was less than 5 mm. Fig. 8c shows the flame propagation process of the Al/B/KNO<sub>3</sub>/PVDF energetic architectures with 1 μm Al powder. All flames jumped and showed larger flame fronts because the energetic sticks containing 10 wt% 1 μm Al powder could release more heat and spray more burning particles during combustion. The flame distance vs. time curves were plotted based on the propagation tracing of flames (Fig. 8d and e). The curves can be divided into two parts: a single-stick combustion zone and an energy coupling zone. The pink square areas represent the propagation trace of flames from single energetic sticks (10 mm stage), with all lines displaying excellent consistency. During the combustion, each energetic stick was surrounded by an energy region composed of heat, gas pressure, and particle advection (Fig. S10 a). When this energy region was close to other energetic sticks and the energy exceeded the ignition thresholds of these sticks, the flame jump phenomenon would occur. Moreover, the capacity to jump was closely related to the distance between the energetic sticks (Fig. S10 b–e) since the energy in this energy region decayed with an increase in the diffusion distance. The lines outside the pink square area represent the flame distance vs. time curves after the occurrence of the flame jump. When the spacings of the energetic architectures were less than 5 mm (B/KNO<sub>3</sub>/PVDF) and 7.5 mm (Al/B/KNO<sub>3</sub>/PVDF), the slopes of the lines changed. The linear burning rates were obtained through linear fitting of lines in this region, as shown in Fig. 8f and g. Rapid combustion occurred in B/KNO<sub>3</sub>/PVDF energetic architectures when the spacing was less than 5 mm, accompanied by an increase in the linear burning rate of the architectures. For Al/B/KNO<sub>3</sub>/PVDF energetic architectures containing 1 μm Al powder, this phenomenon occurred when the spacing was less than 7.5 mm since the added 1 μm Al powder with a content of 10 wt% enhanced the reaction thermodynamic level of the energetic sticks, thereby improving the chemical reaction kinetics of the architectures.

## 4. Conclusion

This study presents the design and preparation of Al/B/KNO<sub>3</sub>/PVDF energetic sticks with different Al particle sizes and different Al contents using the DIW technology. As indicated by the combustion and

oxidation characteristics of fuels, the addition of Al powder can improve the combustion efficiency of B/Al composite fuels and reduce the agglomeration of the combustion products. The slow heating reaction process of the Al/B/KNO<sub>3</sub>/PVDF energetic composites shows that the addition of nano-Al powder can greatly promote the first reaction stage of the reactant and that the addition of micro-Al can primarily promote the second reaction stage of the reactant. The addition of Al powder with content less than 2.5 wt% cannot greatly improve the reactivity of the Al/B/KNO<sub>3</sub>/PVDF composite. In contrast, the addition of a certain amount of Al powder can increase the linear burning rates of the energetic sticks, thereby improving the reaction kinetics of the sticks. The burning rates of the energetic sticks show a decreasing-increasing-decreasing trend with an increase in the 1 μm Al content, while the burning rate vs. Al content curve of energetic sticks containing nano-Al powder lacks troughs. However, the composites with 1 μm Al powder show a higher burning rate than that with nano-Al powder. Similarly, the pressure output tests show that the composites with 1 μm Al powder show higher pressure release and a higher pressurization rate. This may be related to the reaction path of Al powders with different particle sizes. Most interestingly, the jump behavior of flames has been identified during combustion. When the distance between the sticks is below 10 mm, the flames can jump to adjacent sticks. However, the energetic architectures with 10 wt % 1 μm Al powder display a higher reaction rate than the B/KNO<sub>3</sub>/PVDF energetic architecture since the addition of Al powder increases the thermal convection and particle advection between energetic sticks. These findings can be used as a reference for modifying B/KNO<sub>3</sub> energetic composites and regulating the reactivity of energetic sticks.

### Author contribution

Chen-yang Li performed the data analysis and drafted the manuscript. Min-jie Li, Hao-yu Song, and Lei Gao assisted in carrying out the experiments. Chuan-hao Xu and Bao-yun Ye performed the validation. Chong-wei A and Jing-yu Wang performed the review and editing.

### Declaration of competing interest

The authors declare that they have no known competing financial interests or personal relationships that could have appeared to influence the work reported in this paper.

The authors declare the following financial interests/personal relationships which may be considered as potential competing interests.

### Acknowledgments

This work was supported by the National Natural Science Foundation of China (No. 22105184) and the Graduate Education Innovation Project of Shanxi Province (No. 2021Y655).

### Appendix A. Supplementary data

Supplementary data to this article can be found online at <https://doi.org/10.1016/j.enmf.2023.10.004>.

### References

1. Talawar MB, Jangid SK, Nath T, Sinha RK, Asthana SN. New directions in the science and technology of advanced sheet explosive formulations and the key energetic materials used in the processing of sheet explosives: emerging trends. *J Hazard Mater.* 2015;300(30):307–321.
2. Joseph MD, Jangid SK, Satpute RS, et al. Studies on advanced RDX/TATB based low vulnerable sheet explosives with HTPB binder. *Propellants, Explos Pyrotech.* 2009;34(4):326–330.



3. Li Y, Yang Z, Zhang J, et al. Fabrication and characterization of HMX@TPEE energetic microspheres with reduced sensitivity and superior toughness properties. *Compos Sci Technol*. 2017;142(12):253–263.
4. Lin C, Gong F, Qian W, et al. Tunable interfacial interaction intensity: construction of a bio-inspired interface between polydopamine and energetic crystals. *Compos Sci Technol*. 2021;211(28), 108816.
5. Zeng C, Lin C, Zhang J, et al. Grafting hyperbranched polyester on the energetic crystals: enhanced mechanical properties in highly-loaded polymer-based composites. *Compos Sci Technol*. 2019;184(10), 107842.
6. Lysien K, Stolarczyk A, Jarosz T. Solid propellant formulations: a review of recent progress and utilized components. *Materials*. 2021;4(14):6657.
7. Wang D, Cao X, Liu J, et al. TF-Al/TiC highly reactive composite particle for application potential in solid propellants. *Chem Eng J*. 2021;425(1), 130674.
8. Zhang M, Zhao F, Li H, et al. Insight into graphene-salen metal nanocomposites on combustion performance and mechanism of HMX-CMDB propellant. *Chem Eng J*. 2022;429(1), 132175.
9. Qiao Z, Shen J, Wang J, et al. Fast deflagration to detonation transition of energetic material based on a quasi-core/shell structured nanothermite composite. *Compos Sci Technol*. 2015;107(11):113–119.
10. Xu Xu F, Biswas P, Nava G, et al. Tuning the reactivity and energy release rate of  $I_2O_5$  based ternary thermite systems. *Combust Flame*. 2021;228:210–217.
11. Bai C, Li S, Yang D, Li J, Li G, Luo Y. Tremella NiO effectively improve the energy output of Al@NiO nanothermite. *Vacuum*. 2022;207:111553.
12. Zhang Z, Cheng J, Wang Y, et al. Coaxial electrospinning fabrication of core-shell energetic fibers and in-situ integration with SCB exhibiting superior non-contact ignition. *Chem Eng J*. 2023;451(1), 138361.
13. Yu C, Zheng Z, Gu B, et al. Al/lead tetroxide nanothermites for semiconductor bridge applications. *Chem Eng J*. 2023;451(3), 138614.
14. He W, Liu P, He G, Gozin M, Yan Q. Highly reactive metastable intermixed composites (MICs): preparation and characterization. *Adv Mater*. 2018;30(41), 1706293.
15. Khasainov B, Comet M, Veyssiere B, Spitzer D. Comparison of performance of fast-reacting nanothermites and primary explosive. *Propellants, Explos Pyrotech*. 2017;42(7):754–772.
16. Li C, Song H, Xu C, et al. Reactivity regulation of B/ $KNO_3$ /PVDF energetic sticks prepared by direct ink writing. *Chem Eng J*. 2022;450(4), 138376.
17. Sundaram D, Yang V, Yetter RA. Metal-based nanoenergetic materials: synthesis, properties, and applications. *Prog Energy Combust Sci*. 2017;61:293–365.
18. Dreizin EL. Metal-based reactive nanomaterials. *Prog Energy Combust Sci*. 2009;35(2):141–167.
19. Jiang Y, Yilmaz NED, Barker KP, Baek J, Xia Y, Zheng X. Enhancing mechanical and combustion performance of boron/polymer composites via boron particle functionalization. *ACS Appl Mater Interfaces*. 2021;13(24):28908–28915.
20. Hashim SA, Karmakar S, Roy A, Srivastava SK. Regression rates and burning characteristics of boron-loaded paraffin-wax solid fuels in ducted rocket applications. *Combust Flame*. 2018;191:287–297.
21. Yen NH, Wang LY. Reactive metals in explosives. *Propellants, Explos Pyrotech*. 2012;37(2):143–155.
22. Türker L. Thermobaric and enhanced blast explosives (TBX and EBX). *Def. Technol*. 2016;12(6):423–445.
23. Li C, Yan N, Ye Y, et al. Thermal analysis and stability of boron/potassium nitrate pyrotechnic composition at 180°C. *Appl Sci*. 2019;9(17):3630.
24. Hashim SA, Karmakar S, Roy A. Effects of Ti and Mg particles on combustion characteristics of boron-HTPB-based solid fuels for hybrid gas generator in ducted rocket applications. *Acta Astronaut*. 2019;160:125–137.
25. Liang D, Liu J, Zhou Y, Zhou J. Ignition and combustion characteristics of amorphous boron and coated boron particles in oxygen jet. *Combust Flame*. 2017;185:292–300.
26. Liang D, Liu J, Zhou Y, Zhou J, Cen K. Ignition delay kinetic model of boron particle based on bidirectional diffusion mechanism. *Aero Sci Technol*. 2018;73:78–84.
27. Chintersingh KL, Schoenitz M, Dreizin EL. Oxidation kinetics and combustion of boron particles with modified surface. *Combust Flame*. 2016;173:288–295.
28. Hu X, Xu Y, Ao W, Zeng Z, Hua C, Zhu X. Ignition model of boron particle based on the change of oxide layer structure. *Proc Combust Inst*. 2019;37(3):3033–3044.
29. Wang X, Wu T, Wang H, DeLisio JB, Yang Y, Zachariah MR. Boron ignition and combustion with doped  $\delta$ - $B_2O_3$ : bond energy/oxygen vacancy relationships. *Combust Flame*. 2018;197:127–133.
30. Cheng L, Huang C, Yang Y, et al. Preparation and combustion performance of B/PVDF/Al composite microspheres. *Propellants, Explos Pyrotech*. 2020;45(4):657–664.
31. Li C, Wen K, An C, et al. Effect of binder on formability and combustion performance of B/ $KNO_3$  samples by Direct Ink Writing. *Chin J Energetic Mater*. 2022;30(4):332–340.
32. Valluri SK, Schoenitz M, Dreizin E. Bismuth fluoride-coated boron powders as enhanced fuels. *Combust Flame*. 2020;221:1–10.
33. Liu T, Chen X, Xu H, Han A, Ye M, Pan G. Preparation and properties of boron-based nano-B/NiO thermite. *Propellants, Explos Pyrotech*. 2015;40(6):873–879.
34. Mao Y, Zhong L, Zhou X, et al. 3D printing of micro-architected Al/CuO-based nanothermite for enhanced combustion performance. *Adv Eng Mater*. 2019;21(12), 1900825.
35. Hedman TD, Demko AR, Kalman J. Enhanced ignition of milled boron-polytetrafluoroethylene mixtures. *Combust Flame*. 2018;198:112–119.
36. Zhong Q, Li Y, Chen J, Song D. Boron/potassium nitrate microspheres fabricated by electrostatic spraying and their combustion characteristic as pyrotechnic ignitor. *J Therm Anal Calorim*. 2019;138(5):3349–3355.
37. Korotkiy AG, Arkhipov VA, Slyusarsky KV, Sorokin IV. Study of ignition of high-energy materials with boron and Al and titanium diborides. *Combust Explos Shock Waves*. 2018;54:350–356.
38. Zhao W, Wang H, Kline DJ, et al. Influence of titanium addition on performance of boron-based thermites. *Chem Eng J*. 2022;438, 134837.
39. Liu J, Xi J, Yang W, et al. Effect of magnesium on the burning characteristics of boron particles. *Acta Astronaut*. 2014;96:89–96.
40. Cheng L, Yang H, Majeed MA, Li Y, Song D, Li Y. B/Metal composites' thermochemical properties and their effect on the performance of an ammonium perchlorate propellant. *J Energetic Mater*. 2021;39(3):344–360.
41. Wang J, Wang J, Mao Y, Peng R, Nie F. The surface activation of boron to improve ignition and combustion characteristic. *Def. Technol*. 2022;18(9):1679–1687.
42. Wang Y, Li Z, Yu H, Feng C. Reaction mechanism of metastable intermolecular composite. *Prog Chem*. 2016;28(11):1689–1704.
43. Watson KW, Pantoya ML, Levitas VI. Fast reactions with nano-and micrometer Al: a study on oxidation versus fluorination. *Combust Flame*. 2008;155(4):619–634.
44. Badiola C, Schoenitz M, Zhu X, Dreizin EL. Nanocomposite thermite powders prepared by cryomilling. *J Alloys Compd*. 2009;488(1):386–391.
45. Kuntz JD, Cervantes OG, Gash AE, Munir ZA. Tantalum-tungsten oxide thermite composites prepared by sol-gel synthesis and spark plasma sintering. *Combust Flame*. 2010;157(8):1566.
46. Zhang T, Wang Z, Li G, Luo Y. Tuning the reactivity of Al/ $Fe_2O_3$  nanoenergetic materials via an approach combining soft template self-assembly with sol-gel process. *J Solid State Chem*. 2015;230:1–7.
47. Wang H, Zachariah MR, Xie L, Rao G. Ignition and combustion characterization of nano-Al-AP and nano-Al-CuO-AP micro-sized composites produced by electrospray technique. *Energy Proc*. 2015;66:109–112.
48. Jia X, Xu L, Hu Y, et al. Preparation of agglomeration-free composite energetic microspheres taking PMMA-PVA with honeycomb structure as template via the molecular collaborative self-assembly. *J Energetic Mater*. 2021;39(2):182–196.
49. Thiruvengadathan R, Chung SW, Basuray S, et al. A versatile self-assembly approach toward high performance nanoenergetic composite using functionalized graphene. *Langmuir*. 2014;30(22):6556–6564.
50. Severac F, Alphonse P, Esteve A, Bancaud A, Rossi C. High-energy Al/CuO nanocomposites obtained by DNA-directed assembly. *Adv Funct Mater*. 2012;22(2):323–329.
51. Chandru RA, Balasubramanian N, Oommen C, Raghunandan BN. Additive manufacturing of solid rocket propellant grains. *J Propul Power*. 2018;34(4):1090–1092.
52. Straathof MH, Driel CA, Lingen JNJ, Ingenhous BLJ, Cate AT, Maalderink HH. Development of propellant compositions for vat photopolymerization additive manufacturing. *Propellants, Explos Pyrotech*. 2020;45(1):36–52.
53. Yang W, Hu R, Zheng L, Yan G, Yan W. Fabrication and investigation of 3D-printed gun propellants. *Mater Des*. 2020;192, 108761.
54. Wang D, Zheng B, Guo C, et al. Formulation and performance of functional sub-micro CL-20-based energetic polymer composites ink for direct-write assembly. *RSC Adv*. 2016;6(113):112325–112331.
55. Ye B, Song C, Huang H, Li Q, An C, Wang J. Direct ink writing of 3D-Honeycombed CL-20 structures with low critical size. *Def. Technol*. 2020;16(3):588–595.
56. Xie Z, An C, Ye B, et al. 3D direct writing and micro detonation of CL-20 based explosive ink containing O/W emulsion binder. *Def. Technol*. 2022;18(8):1340–1348.
57. Li C, Kong S, Liao D, An C, Ye B, Wang J. Fabrication and characterization of mussel-inspired layer-by-layer assembled CL-20-based energetic films via micro-jet printing. *Def. Technol*. 2022;18(10):1748–1759.
58. Zheng D, Huang T, Xu B, et al. 3D printing of n-Al/polytetrafluoroethylene-based energy composites with excellent combustion stability. *Adv Eng Mater*. 2021;23(5), 2001252.
59. Wang H, Shen J, Kline DJ, et al. Direct writing of a 90 wt% particle loading nanothermite. *Adv Mater*. 2019;31(23), 1806575.
60. Wang H, Kline DJ, Biswas P, Zachariah MR. Connecting agglomeration and burn rate in a thermite reaction: role of oxidizer morphology. *Combust Flame*. 2021;231, 111492.
61. Xu C, Zhao Z, Qiao Z, et al. Reactivity of nanothermite-based micro energetic sticks prepared by direct ink writing. *Chem Eng J*. 2022;438, 135608.
62. Wainwright ER, Sullivan KT, Grapes MD. Designer direct ink write 3D-printed thermites with tunable energy release rates. *Adv Eng Mater*. 2020;22(6), 1901196.
63. Xu J, Chen Y, Zhang W, et al. Direct ink writing of nAl/pCuO/HPMC with outstanding combustion performance and ignition performance. *Combust Flame*. 2022;226, 111747.
64. Murray AK, Novotny WA, Fleck TJ, et al. Selectively-deposited energetic materials: a feasibility study of the piezoelectric inkjet printing of nanothermites. *Addit Manuf*. 2018;22:69–74.
65. Levitas VI, Asay BW, Son SF, Pantoya M. Melt dispersion mechanism for fast reaction of nanothermites. *Appl Phys Lett*. 2016;89(7), 071909.
66. Levitas VI, Asay BW, Son SF, Pantoya M. Mechanochemical mechanism for fast reaction of metastable intermolecular composites based on dispersion of liquid metal. *J Appl Phys*. 2007;101, 083524.

67. Gao D, Wei X, Liu J, et al. Laser ignition and combustion characteristics of B-Al compound powder without and with HMX: a comparative study. *Aero Sci Technol.* 2022;120, 107268.
68. Ao W, Zhou J, Liu J, Yang W, Wang Y, Li H. Kinetic model of single boron particle ignition based upon both oxygen and (BO)<sub>n</sub> diffusion mechanism. *Combust Explos Shock Waves.* 2014;50:262–271.
69. Liang D, Liu J, Zhou Y, Zhou J, Cen K. Ignition delay kinetic model of boron particle based on bidirectional diffusion mechanism. *Aero Sci Technol.* 2018;73:78–84.
70. Hu X, Xu Y, Ao W, Zeng Z, Hu C, Zhu X. Ignition model of boron particle based on the change of oxide layer structure. *Proc Combust Inst.* 2019;37(3):3033–3044.
71. Wainwright ER, Sullivan KT, Grapes MD. Designer direct ink write 3D-printed thermites with tunable energy release rates. *Adv Eng Mater.* 2020;22(6), 1901196.
72. Sullivan KT, Zhu C, Duoss EB, et al. Controlling material reactivity using architecture. *Adv Mater.* 2016;28(10):1934–1939.



**Chen-yang Li**, a doctor majoring in Environmental and Safety Engineering at the North University of China, is a National Scholarship winner. His research interests include the modification of energetic materials and the 3D printing technology for energetic materials. Email: [lichenyang\\_nuc@163.com](mailto:lichenyang_nuc@163.com)



**Chong-wei A** is a doctoral supervisor at the North University of China, Director of the Department of Weaponry Science and Technology of the university, Deputy Director of the Shanxi Engineering Technology Research Center for Ultrafine Powder, and an outstanding young academic leader of the Shanxi higher education institutions. Furthermore, he also serves as a member of the Pyrotechnics and Pyrotechnics Subcommittee of the China Ordnance Society and Director of the Special Micro-Nano Devices and Systems Subcommittee of the China Micro-Nano Technology Society. He has been honored with a national excellent thesis instructor for a master's degree in the China Ordnance Society and 2022 Highly Cited Chinese Researchers by Elsevier. His research interests include new booster technology for explosives, technology for energetic compound modification, and 3D printing technology. Email: [anchongwei@yeah.net](mailto:anchongwei@yeah.net)